

Some observations on vortex-ring collisions upon inclined surfaces

T. H. New¹  · Shengxian Shi² · B. Zang¹

Received: 15 January 2016 / Revised: 1 June 2016 / Accepted: 2 June 2016 / Published online: 13 June 2016
© Springer-Verlag Berlin Heidelberg 2016

Abstract This paper reports upon a laser-induced fluorescence visualization and time-resolved particle image velocimetry study to resolve the detailed dynamics associated with $Re = 2000$ and 4000 circular vortex rings colliding with 30° – 75° inclined surfaces. Two-dimensional visualization results show that larger inclination angles lead to increasingly rapid size reduction in the primary vortex-ring core closer to the surface, faster formation of the secondary vortex-ring core, and subsequent ingestion by the former. In contrast, primary vortex-ring core further away from the surface becomes physically larger and incoherent more rapidly, with slower formation and entrainment of the secondary vortex-ring core. Interestingly, a vortex dipole and small vortex-ring-like structure are produced for the largest inclination angle of 75° , possibly due to vortex disconnection and reconnection processes. Results taken along the non-inclined plane show significant bulging of the primary vortex-ring cores when the inclination angle increases from 30° onwards. More importantly, additional vortex cores are observed to entwine with the primary vortex-ring core and provide strong direct evidence for the bi-helical vortex line flow mechanism put forward by Lim (Exp Fluids

7:453–463, 1989). Lastly, the behaviour of the primary and secondary vortex-ring cores further away from the surface is highly sensitive towards the state of the bi-helical lines compressed at that region. Strong compression driven by circumferential flows due to large inclination angles may explain the unique flow structures and behaviour observed for 75° inclination angle here.

1 Introduction

Collision of circular vortex rings upon solid boundaries has seen many systematic experimental and numerical investigations since more than three decades ago. Not only does this flow scenario pose intriguing questions regarding the highly dynamic flow changes to the vortex ring and wall boundary layer during the collision, it is also relevant towards better understanding of circular jets impinging upon solid boundaries as well. The latter flow situation is particularly relevant towards the engineering usage of impinging jets in areas such as aircraft deicing, cooling of gas turbine components, as well as cooling of electrical components during the manufacturing process, amongst many other industrial applications. Studies on “head-on” or inclined collisions between vortex rings and flat surfaces have been conducted and well documented by Walker et al. (1987), Homa et al. (1988), Lim (1989), Orlandi (1990), Lim et al. (1991), Orlandi and Verzicco (1993), Verzicco and Orlandi (1994), Swearingen et al. (1995), Chu et al. (1995), Jang et al. (1996), Fabris et al. (1996), Minota et al. (1997), Naitoh et al. (2001), Adhikari and Lim (2009), Cheng et al. (2010), Couch and Krueger (2011), Hrynyuk et al. (2012), and Naaktgeboren et al. (2012), just to name a few selected studies.

The present study was motivated by investigations carried out by Lim (1989) and Couch and Krueger (2011). The

Electronic supplementary material The online version of this article (doi:10.1007/s00348-016-2196-7) contains supplementary material, which is available to authorized users.

✉ T. H. New
dthnew@ntu.edu.sg

¹ School of Mechanical and Aerospace Engineering, Nanyang Technological University, 50 Nanyang Avenue, Singapore, Singapore

² Gas Turbine Research Institute, School of Mechanical Engineering, Shanghai Jiao Tong University, Shanghai 200240, China

former study provided us with one of the first detailed look at how the vortex lines associated with the circular vortex ring could be interpreted as a transition into bi-helical mode, where the bi-helical vortex lines entwine and propagate along the vortex-ring circumferential axis, after the vortex ring collides with an inclined surface. At this point, it is worthwhile to clarify that the vortex ring can be treated as a circular vortex filament and the core of the vortex ring (i.e. vortex core) refers to the 2D cross section of the circular vortex filament. Based on the top- and side-view visualizations obtained during that investigation, it was put forward that as the vortex ring approaches the inclined surface, higher vortex-stretching levels will be conferred upon the vortex filament section closer to the surface than that further away from the surface. This gives rise to non-uniform vortex-core size distribution along the vortex-ring filament, resulting in vortex lines winding around the vortex-ring circumferential axis. This further leads to the formation of bi-helical lines where the winding direction of the vortex lines is symmetrical about the plane of symmetry, as shown in Fig. 1a.

As the collision process progresses, the bi-helical lines will gradually move from the vortex-ring section closer to the surface to that further away from the surface, such that they are finally compressed at the latter location, as shown in Fig. 1b. For more details, readers are advised to refer to Lim (1989) and it should be noted that these figures correspond to the two-dimensional sketches included in Figs. 10(e) and 10(f) in Lim (1989). That earlier study successfully demonstrated that the presence of a solid boundary is essential towards the compression of the bi-helical lines and formation of secondary vortex rings. However, the study by Lim (1989) was also limited to a single inclination angle of 51.5° , and the Reynolds numbers used were comparatively low at $Re = 600\text{--}2000$. As such, the effects

of inclination angle upon the vortex-stretching effects, bi-helical vortex lines, and secondary vortex rings remain largely unexplored in that study. Furthermore, the presence and behaviour of bi-helical vortex lines have not been directly observed under different inclination angles as well.

In a more recent study by Couch and Krueger (2011), they investigated $Re = 2000\text{--}4000$ vortex-ring collisions at different inclination angles using laser-induced fluorescence (LIF), digital particle image velocimetry (DPIV), and defocusing digital particle tracking velocimetry (DDPTV). It can be appreciated that the investigation primarily made use of quantitative flow measurements to elucidate the flow dynamics. And while their study provided significant quantitative information upon the effects of inclination angle on the vortex-ring collision behaviour (amongst other parameters), the more salient and transient dynamics of the collision process could not be discerned very clearly from their limited flow visualizations. This might be either due to rapid diffusion of the fluorescent dye that highlighted the vortex-ring streamlines or the use of band-pass lens filter to reduce scattered laser light during that study. Though DPIV results were presented for the collision processes associated with different inclinations angles, the DPIV system was only operating at a moderate sampling frequency. Arguably, flow visualizations captured at higher frame rates may be more intuitive under some circumstances in terms of resolving the more salient flow dynamics. Due to the highly dynamic nature of vortex-ring collisions with solid boundaries, it will then be desirable to capture the entire vortex-ring collision processes under different configurations in greater clarity. Lastly, as the focus of the study was not to look into the overall vortex-ring collision mechanism, the bi-helical vortex line mechanism put forward by Lim (1989) was not discussed in detail.

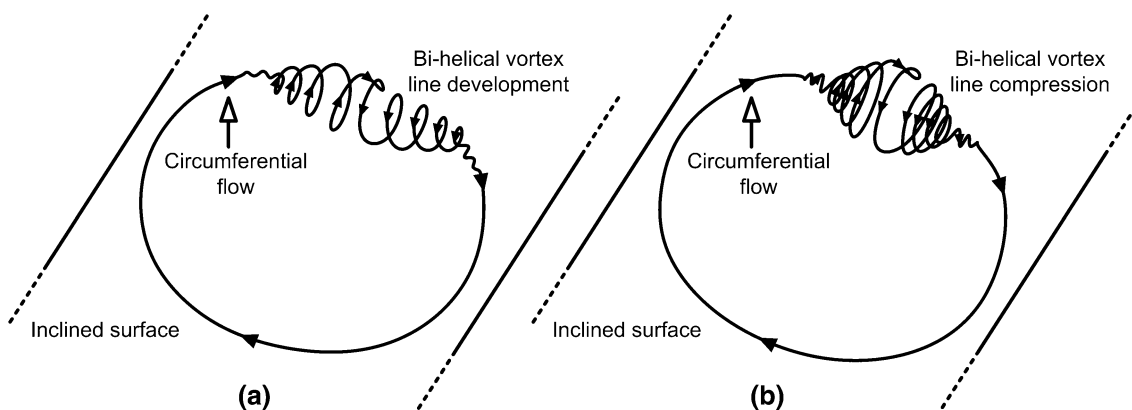


Fig. 1 3D sketches of the bi-helical vortex line (a) development, and subsequent (b) compression as a vortex ring collides upon an inclined surface, in accordance with the flow model put forward by Lim (1989) previously

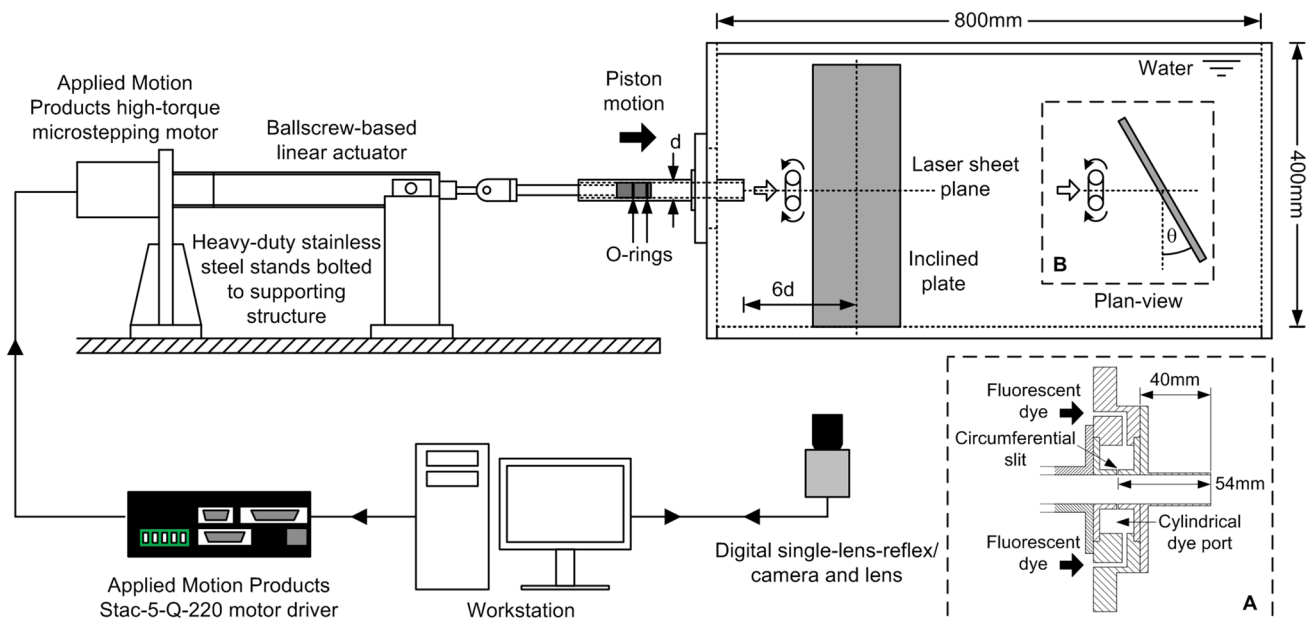


Fig. 2 Schematics of the vortex-ring collision with inclined surface experimental set-up

With the above in mind, the present authors conducted a more detailed flow visualization and measurement study to complement the investigations carried out by Lim (1989) and Couch and Krueger (2011) previously. As a result, special attention was paid during the present study to fine-tune the flow visualization and measurement procedures, such that dynamical changes to the vortex ring during the collision processes can be clearly discerned. It should be stressed here that much of the fundamental dynamics of vortex-ring collisions upon inclined surfaces have been well covered by earlier studies, and this paper will not be presenting all the experimental results in detail. Instead, only the more interesting flow differences revealed and clarified by the present flow visualization experiments, which might not have been observed too clearly in previous studies, will be presented and discussed. In particular, the effects of inclination angle upon the primary and secondary vortex rings in relation to the bi-helical vortex line model, their behaviour during the collision, and vortex-core trajectories will be the primary focus. As a matter of consistency and ease in comparisons, the present study will make use of vortex-ring Reynolds numbers similar to those used by Couch and Krueger (2011).

2 Experimental set-up and procedures

The experimental set-up made use of a water tank-based set-up, comprising of a Bosch 10-mm pitch ball screw linear actuator coupled to an Applied Motion Products

high-torque microstepping stepper motor and driver system, as shown in Fig. 2. The motor driver was controlled by a workstation such that each motor revolution required 51,200 microsteps to complete and thus provided high-resolution motion control options. The working end of the linear actuator was connected to a smooth Delrin-based cylindrical piston fitted snugly into a hollow stainless steel cylinder with an internal diameter of 20 mm. The hollow cylinder was in turn securely attached to a circular Plexiglas attachment with a 20-mm-diameter borehole. The former was fabricated to house a cylindrical dye port for releasing fluorescent dye through a 1 mm circumferential gap for visualization purposes (see inset A of Fig. 2), where the circumferential gap was located at 54 mm upstream of a circular nozzle exit (i.e. more details to be provided later). Circumferential release of fluorescent dye into the cylinder proved to be crucial in terms of achieving more homogenous dye distributions in the visualized vortex rings. The circular Plexiglas attachment then sat flushed within a circular cut-out in one of water tank walls and bolted securely. Finally, a 40-mm-long $d = 20$ -mm internal diameter circular nozzle was fixed to Plexiglas attachment, such that the entire flow path from the piston to the nozzle was 20 mm in diameter throughout. The purpose of using a circular nozzle was to minimize wall proximity effects coming off from the tank wall. The linear actuator system and water tank were bolted down to the test stand via heavy-duty stainless steel stands to prevent any jerking actions that might interfere with the vortex-ring generation and collision behaviour.

All vortex rings were produced via the “cylindrical slug” technique, where the linear actuator was programmed to drive the piston forward based on trapezoidal velocity profiles. They were generated at Reynolds numbers of $Re = Ud/\nu = 2000$ and 4000 , where U and ν were based on water working conditions during the experiments. To avoid exceeding the vortex-ring formation length and thus formation of trailing jets which might interfere with the undisturbed vortex-ring dynamics, a piston stroke length of $L = 30$ mm was used. This corresponds to a stroke ratio of $L/d = 1.5$, which is significantly smaller than that associated with trailing jet formations (Gharib et al 1998; Krueger and Gharib 2003) and remains within the range used by Couch and Krueger (2011) as well. A 20-mm-thick flat plate served as the impingement surface as shown in Fig. 1 and was securely seated on the water tank bottom surface at a mean separation distance of $6d$ away from the nozzle exit. For the present study, the flat surface was inclined at $\theta = 0^\circ$ (i.e. head-on collision), 30° , 45° , 60° , and 75° (see plan view of flat plate in inset B of Fig. 2). To minimize light-scattering during the experiments and to enhance contrast, thin matte black adhesive paper was used to cover the impingement side of the flat plate. During all experiments, the 400 mm (W) \times 400 mm (H) \times 800 mm (L) water tank was filled up to a height of approximately 380 mm and completely covered the flat plate to minimize any free surface effects.

To visualize the dynamic behaviour of the vortex-ring collisions clearly, LIF visualizations were performed. The experimental set-up and procedures were relatively similar to those adopted by New and Tay (2006) and New and Tsovolos (2009). Fluorescein disodium dye was premixed with water before it was introduced into and released out of the circumferential slit of the cylindrical port prior to the vortex-ring generation. The excitation source was a CNI 8W, 532-nm wavelength diode-pumped solid-state (DPSS) laser, from which a thin laser sheet of approximately 1 mm thickness was produced by sheet-forming optics. The laser sheet was aligned such that it was located either along the inclined surface (i.e. inclined plane) or a plane orthogonal to that (i.e. non-inclined plane) to visualize the flow behaviour accordingly. Flow visualizations were captured using a remotely controlled Canon digital single-lens reflex camera with a 50 mm, $f/1.4$ lens, where it was located either below or beside the transparent water tank to record the flow behaviour along the appropriate visualization planes. To ensure that even the smaller vortex structures could be captured clearly, all visualizations were captured in 30 frames-per-second videos at 1920 px \times 1080 px resolution. Furthermore, camera focusing, exposure time, and aperture were adjusted remotely on the workstation to minimize disturbances to the set-up. For the purpose of discussions within this paper, static flow images were extracted from

the video-recordings and included here. On the other hand, segments of video-recordings have also been included here as supplementary material for playback purposes.

To validate and complement the flow visualizations, time-resolved particle image velocimetry (TR-PIV) measurements had also been taken, with procedures similar to those adopted by Shi and New (2013), Shi et al. (2013), and New et al. (2013) previously. The use of TR-PIV here allows further appreciation of the highly dynamic vortical changes during the collision process, due to its ability to resolve minute flow changes quantitatively. The above-mentioned laser sheet was used to illuminate 20- μ m-sized hollow glass spheres that were uniformly distributed within the water tank prior to the TR-PIV experiments. An IDT high-speed CMOS camera of 1024 px \times 1024 px resolution with a 50 mm, $f/1.4$ lens was used to capture light reflected off the particles at an acquisition speed of 200 frames per second with an exposure time of 2.5 ms. The workstation-controlled camera was triggered at the same time when the vortex-ring generator started to initiate during the experiments and about 2000 images were captured into the camera buffer for each experimental run. These images were subsequently transferred to the workstation for post-processing to obtain the velocity fields and other results. To ensure satisfactory accuracy in the TR-PIV measurement results, the experiments were performed along guidelines recommended by Keane and Adrian (1992). For instance, particle shifts between consecutive images were kept to within 20 % of the final interrogation window size and that there were approximately 5–10 particles found in the smallest interrogation window.

Images were processed consecutively such that images i and $i + 1$ were taken as the image pairs with a constant time interval of $\Delta t = 4$ ms. This led to displacements (i.e. $\Delta x = U\Delta t$) of 0.4 and 0.8 mm for reference velocities associated with $Re = 2000$ and 4000 test cases, respectively, between two consecutive velocity vector fields of the present TR-PIV measurements. Processing of the captured particle images was based on multigrid cross correlations with initial and final interrogation window sizes of 128 px \times 128 px and 32 px \times 32 px, respectively. Window overlaps in the horizontal and vertical directions were maintained at 50 % throughout as well. Raw velocity fields were validated via a 3-point by 3-point neighbour validation scheme, where spurious vectors were replaced by vectors determined by an averaging filter to arrive at the final velocity fields. The vector spacing and spatial resolution of the present DPIV measurement results were approximately 1.76 mm \times 1.76 mm in both horizontal and vertical directions of the velocity field results, respectively. The exact number of vector replacements depended on the exact velocity field, but typically about 1 % of the velocity vectors in the velocity field was replaced through the

validation and neighbourhood averaging procedures. Most of these replaced spurious vectors were located near the inclined surface boundary captured in the particle images, where more particles tend to move out of the measurement plane because of the highly three-dimensional vortex-ring collision process.

Subsequently, other derived quantities such as vorticity results were determined from these velocity field results. The vorticity results were calculated based on central-differencing implementations of $\vec{\omega} = \nabla \times \vec{u}$, and the uncertainty level in the vorticity results was estimated to be approximately $\pm 3.4\%$ (Luff et al. 1999). It should be mentioned that these vorticity results have been compared to λ_2 -criterion filtered results, and both of them proved to be capable of capturing all the dominant vortex cores. However, since the vorticity results are also capable of highlighting wall boundary layer separations much better than λ_2 -criterion filtered results, the former will be presented here for a better appreciation of the flow fields instead. Lastly, due to significant similarities between the present TR-PIV procedures and those used earlier on, readers are referred to the earlier studies for estimates of other experimental uncertainties (Shi and New 2013; New et al. 2013).

3 Results and discussion

3.1 Head-on collision with flat surface

As a matter of reference for other vortex-ring collision configurations, Figs. 3 and 4 show the flow visualizations and TR-PIV out-of-plane vorticity (i.e. ω_z) results associated with a $Re = 2000$ vortex ring colliding head-on against a flat surface (i.e. $\theta = 0^\circ$). For the sake of brevity, note that the

flow images were extracted to highlight the important flow changes only. Readers may refer to the “ $Re = 2000$ head-on collision” and “ $Re = 2000$ head-on collision TR-PIV” videos encoded at 15 and 20 frames per second (i.e. see Supplementary materials 1 and 2 respectively), for a more detailed look at the entire flow sequences. Additionally, results in Figs. 3 and 4 are selected such that they are matched as closely as possible and that the time points were non-dimensionalized similarly to Couch and Krueger (2011), where $\tau = tU/d$. Even though two different Reynolds numbers of $Re = 2000$ and 4000 were investigated, results associated with $Re = 2000$ will mostly be presented here. General vortex-ring collision behaviour associated with $Re = 2000$ appears to evolve slower, temporally speaking, but remain largely similar to that of $Re = 4000$ test case.

Returning to the figure, it can be observed that the primary vortex ring becomes increasingly flattened and its core-to-core diameter increases during the very early stages of the collision, as shown in Figs. 3a, b and 4a, b. The increasingly larger radial extent of the primary vortex ring eventually leads to the separation of the wall boundary layer under the influence of an adverse pressure gradient along the flat surface around the primary vortex-ring periphery as shown in Figs. 3c and 4c, which subsequently rolls up into a secondary vortex ring of opposite vorticity (see Figs. 3d, 4d). As these events unfold, part of the primary vortex-ring cores shown in Fig. 3e–h can be seen to experience significant flow shearing along the flat surface. The primary vortex ring proceeds to entrain the secondary vortex ring such that the latter leapfrogs over the former and resides within its confines, with a corresponding reduction in the secondary vortex-ring core-to-core diameter. This behaviour is depicted in Figs. 3e–g and 4e–g, where the primary and secondary vortex-ring cores lift off from

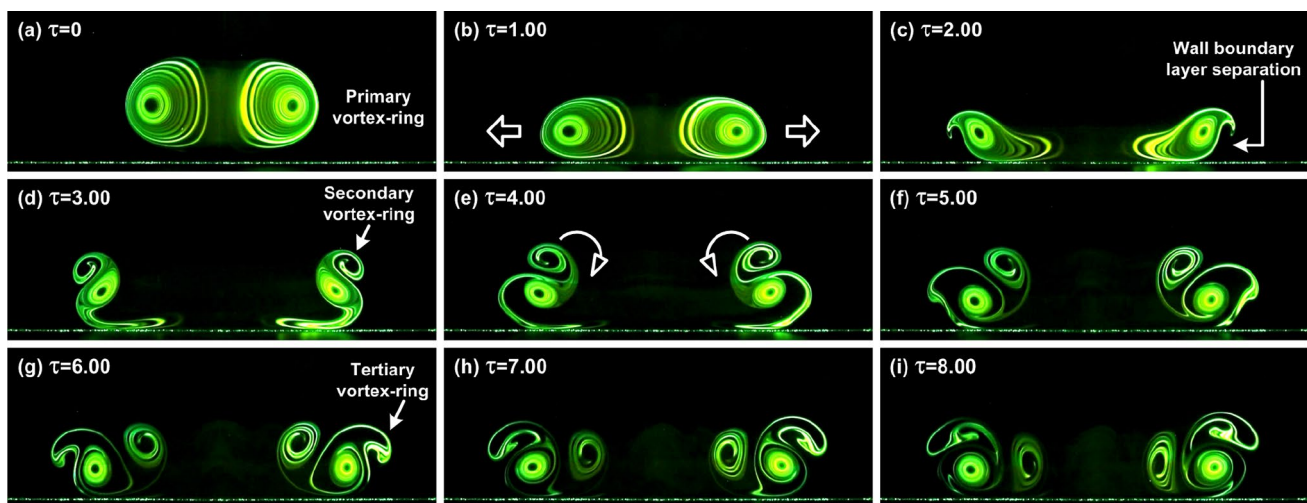


Fig. 3 Instantaneous flow visualizations of $Re = 2000$ vortex ring colliding head-on with flat surface

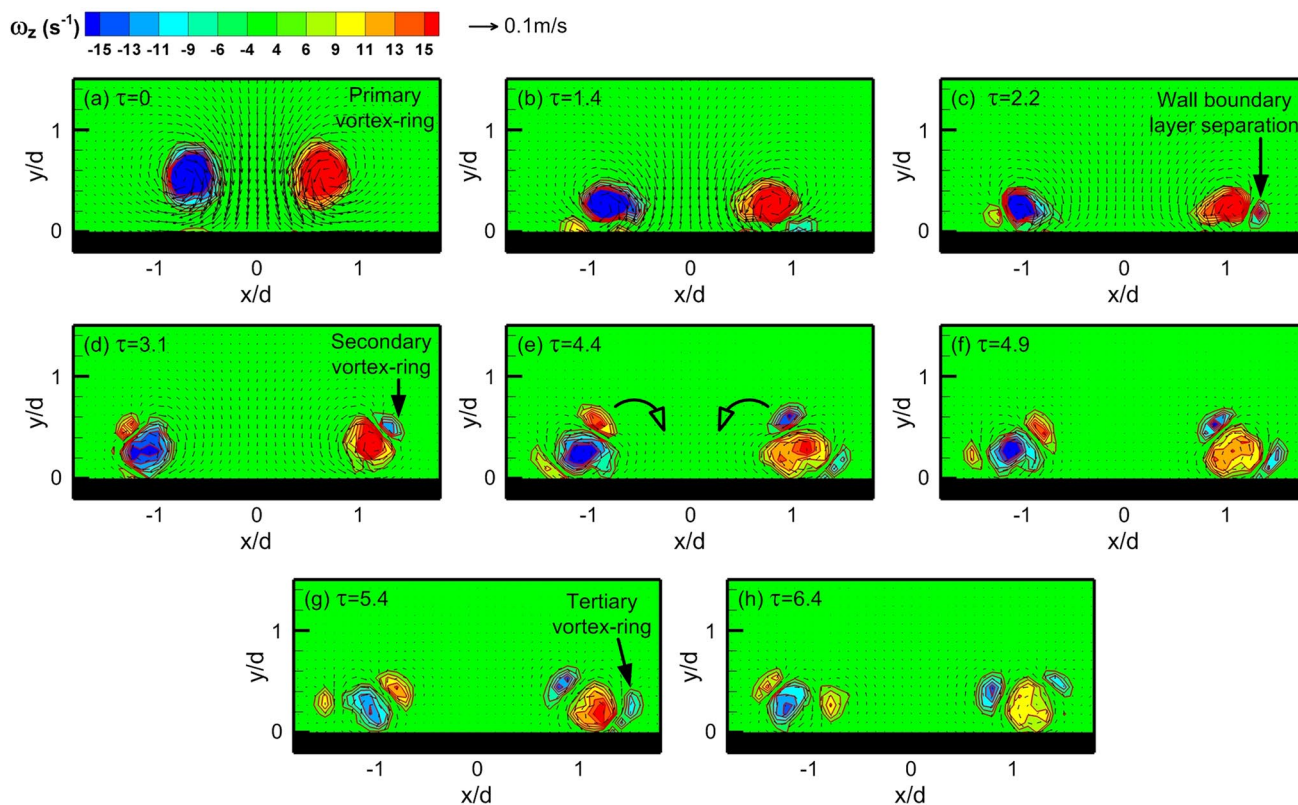


Fig. 4 Instantaneous vorticity maps of $Re = 2000$ vortex ring colliding head-on with flat surface

the surface and rotate towards the collision axis, before returning to the surface again.

At this point, Figs. 3g–i and 4g, h show that a tertiary vortex ring forms along the primary vortex-ring periphery and leapfrogs the primary vortex ring, much like what has been observed for the secondary vortex ring. However, due to the presence of the secondary vortex ring within the primary vortex-ring confines, the tertiary vortex ring is not engulfed entirely by the latter. From the vortex-core motions depicted in these and other flow visualization images presented later, trajectories of the primary and secondary vortex cores could be determined reliably from the still images extracted from the recorded video files and presented for discussions later. Despite the inherent differences between various experimental techniques, there are excellent agreements between the flow phenomenon shown in Figs. 3 and 4 with those observed by Walker et al. (1987), Lim (1989), Lim et al. (1991), Orlandi and Verzico (1993), Cheng et al. (2010), and Couch and Krueger (2011).

3.2 Collision behaviour along inclined plane

Figures 5 and 6 show the visualization images and vorticity maps taken for a vortex ring colliding upon a flat surface that

was inclined at a moderate angle of 30° (see “ $Re = 2000$ 30° inclined collision – inclined plane” and “ $Re = 2000$ 30° inclined collision – inclined plane TR-PIV” video clips in Supplementary materials 3 and 4 respectively). For ease and clarity in explaining subsequent flow developments associated with the different vortex structures, the visualized cores of the same primary vortex ring through these 2D LIF visualizations will be denoted as vortex cores *A* and *B*, where the former and latter are located closer to and further away from the inclined surface, respectively. They will correspond to the lower/upstream and upper/downstream vortex core nomenclature used by Couch and Krueger (2011). Since vortex core *A* collides with the inclined surface before vortex core *B* does, the wall boundary layer separates and produces a secondary vortex core, which vortex core *A* quickly entrains (see Figs. 5d–f, 6c–f). Subsequently, Figs. 5f–i and 6f–i show that vortex core *B* collides upon the inclined surface eventually, followed by the formation of another secondary vortex core and its entrainment by vortex core *B*. It is worthwhile to mention that vortex core *A* reduces remarkably in size during the preceding flow events, presumably due to vortex-stretching effects as it travels up the inclined surface while vortex core *B* continues to travel down the inclined surface. At the same time, part of vortex core *A* is being entrained by vortex core *B* along the inclined surface

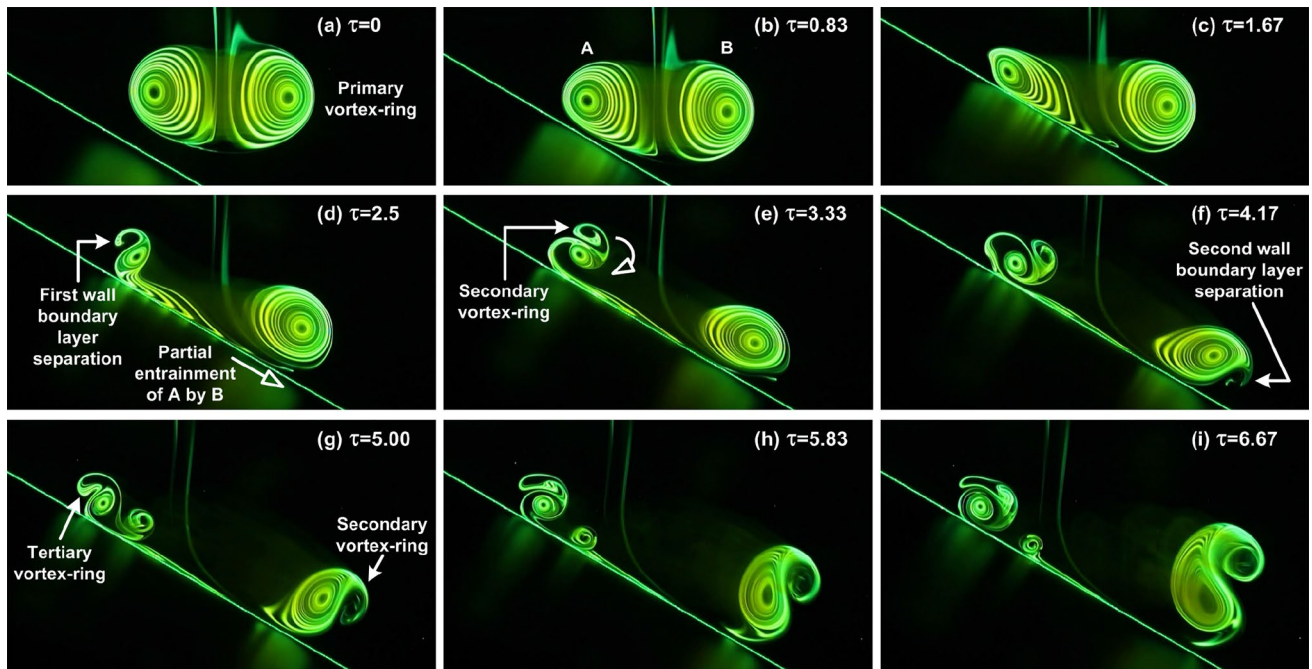


Fig. 5 Instantaneous flow visualizations of $Re = 2000$ vortex-ring collision with 30° inclined flat surface as viewed along the inclined plane

(see Figs. 5d, 6c) through a shearing action, which further attests to the vortex-stretching effects experienced by vortex cores *A* and *B*. Lastly, it should not escape the readers' attention as well that there exist significant differences in the lengthscales and timescales of the flow changes associated with vortex cores *A* and *B*.

For instance, vortex core *B* and the adjacent secondary vortex core are physically larger than vortex core *A* and the secondary vortex core adjacent to it. In fact, as vortex core *B* entrains the secondary vortex core, both of them increase in physical size with the vortex core *B* becoming significantly larger and less coherent. These results support the notion put forward by Lim (1989) that vortex-stretching is non-uniform along the entire primary vortex ring, with highest and lowest levels occurring along vortex cores *A* and *B*, respectively. As such, compression of vortex lines is expected at the vortex core *B* region and should that happens, it may lead to flow behaviour resembling the bi-helical vortex lines flow mechanism put forward in that study. It is also interesting to note now that the invariance of the phenomenon associated with vortex-ring collision upon inclined surface between the present study and Lim (1989), despite the significant differences in the vortex-ring Reynolds number and inclination angle. This gives confidence that flow visualizations obtained at other inclination angles and orientations will shed light upon how bi-helical vortex lines may be formed along the primary vortex-ring circumferential axis as the inclination angle becomes increasingly larger. With this in mind, flow visualization results for a

larger inclination angle will now be presented. However, only more interesting flow differences will be highlighted and compared instead of describing the entire flow dynamics again.

Figures 7 and 8 show corresponding results for the collision of a vortex ring against a 60° inclined surface (see “ $Re = 2000$ 60° inclined collision – inclined plane” and “ $Re = 2000$ 60° inclined collision – inclined plane TR-PIV” video clips in Supplementary materials 5 and 6 respectively). It can be observed that the gross flow phenomenon exhibited by these increasingly larger inclination angles remains largely similar with the previous 30° inclination test case. Note that while other inclination angles of 45° and 75° were experimented upon as well, the general flow behaviour are quite similar and their results are omitted here for the sake of brevity. Closer inspection of these results however will reveal a few interesting observations when the inclination angle doubles here. Firstly, the fundamental behaviour associated with the collision of vortex core *A* upon the inclined surface is invariant to the exact inclination angle used. This is apparent when vortex core *A* and the secondary vortex core adjacent to it are examined in Figs. 7a–e and 8a–d. In contrast, an increase in the inclination angle will see vortex core *B* becoming incoherent faster after the collision. In particular, the transition to flow incoherence resembles a vortex breakdown-like phenomenon, with a rapid increase in vortex core *B* diameter and loss of clarity of its initially coherent dye streaks. Secondly, secondary vortex-core formation and its entrainment

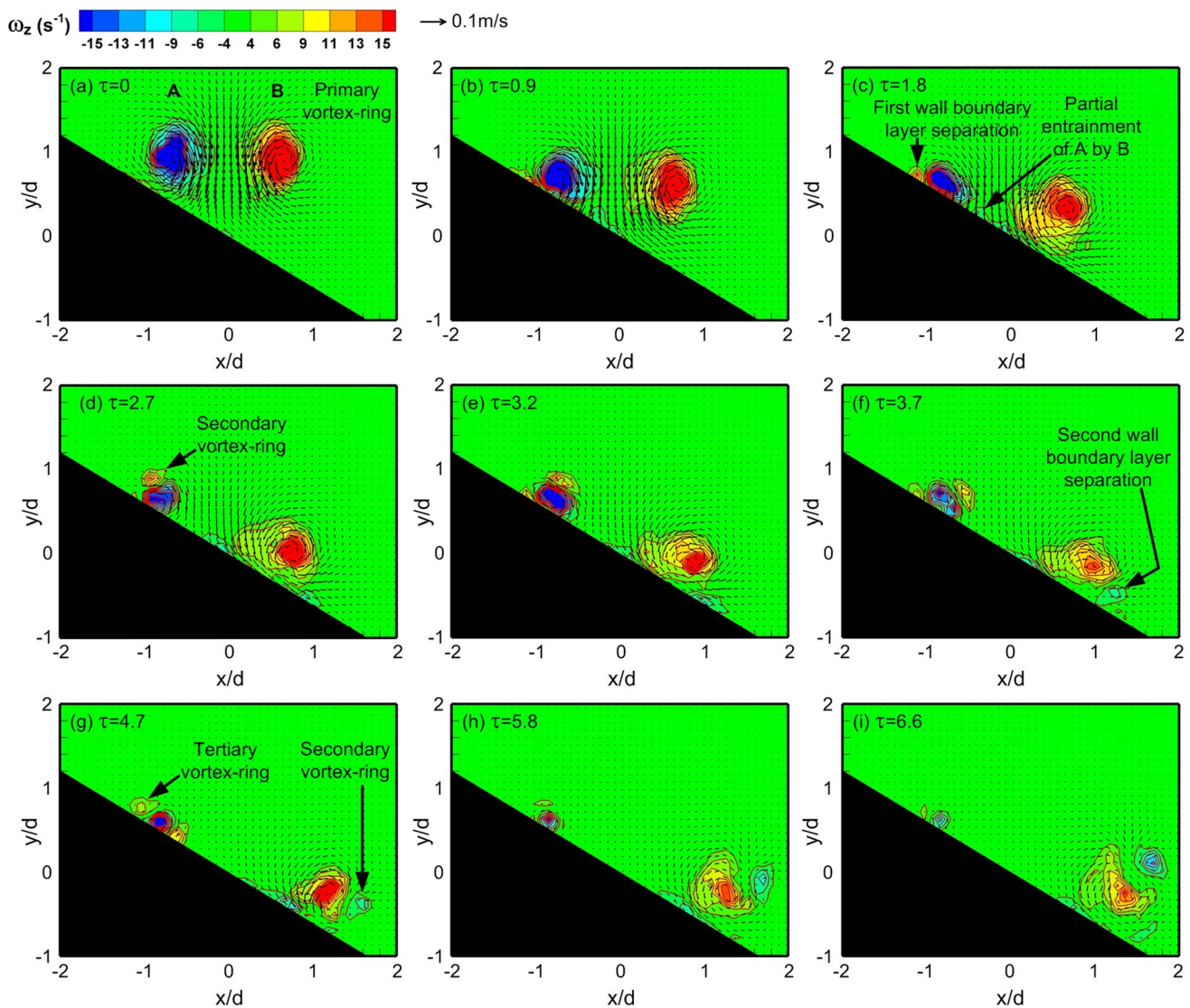


Fig. 6 Instantaneous vorticity maps of $Re = 2000$ vortex ring colliding with 30° inclined flat surface as viewed along the inclined plane

by vortex core *A* occur over increasingly shorter time spans as the inclination angle increases. On the other hand, the time taken for the secondary vortex core to be formed and entrained by vortex core *B* becomes progressively longer with similar increments in the inclination angle. In fact, entrainment of the secondary vortex core by vortex core *B* becomes progressively weaker and slower as the inclination angle increases, as can be seen in Figs. 7 and 8.

Lastly, the physical size of vortex core *A* after entrainment of the secondary vortex core becomes smaller at increased rates as the inclination angle becomes larger. They remain attached to the inclined surface after the collisions as small isolated vortices which ultimately diffuse through viscous effects, with a diffusion rate that is qualitatively observed to increase with the inclination angle used. Based on the bi-helical vortex line framework put forward

by Lim (1989), differences in the vortex-stretching levels experienced by vortex cores *A* and *B* become greater with increasing inclination angle, such that circumferential flow from vortex core *A* to vortex core *B* increases correspondingly. This in turn produces a stronger compression of the bi-helical vortex lines upon vortex core *B* and will lead to its faster breaking down. As such, flow visualization results presented so far can be seen to be in good agreements with the bi-helical vortex line model.

3.3 Effects of vortex-ring Reynolds number

The preceding agreement extends to the case when the vortex-ring Reynolds number increases to $Re = 4000$. This can be appreciated in Figs. 9 and 10, where flow visualizations for collisions of $Re = 4000$ vortex rings against a 30°

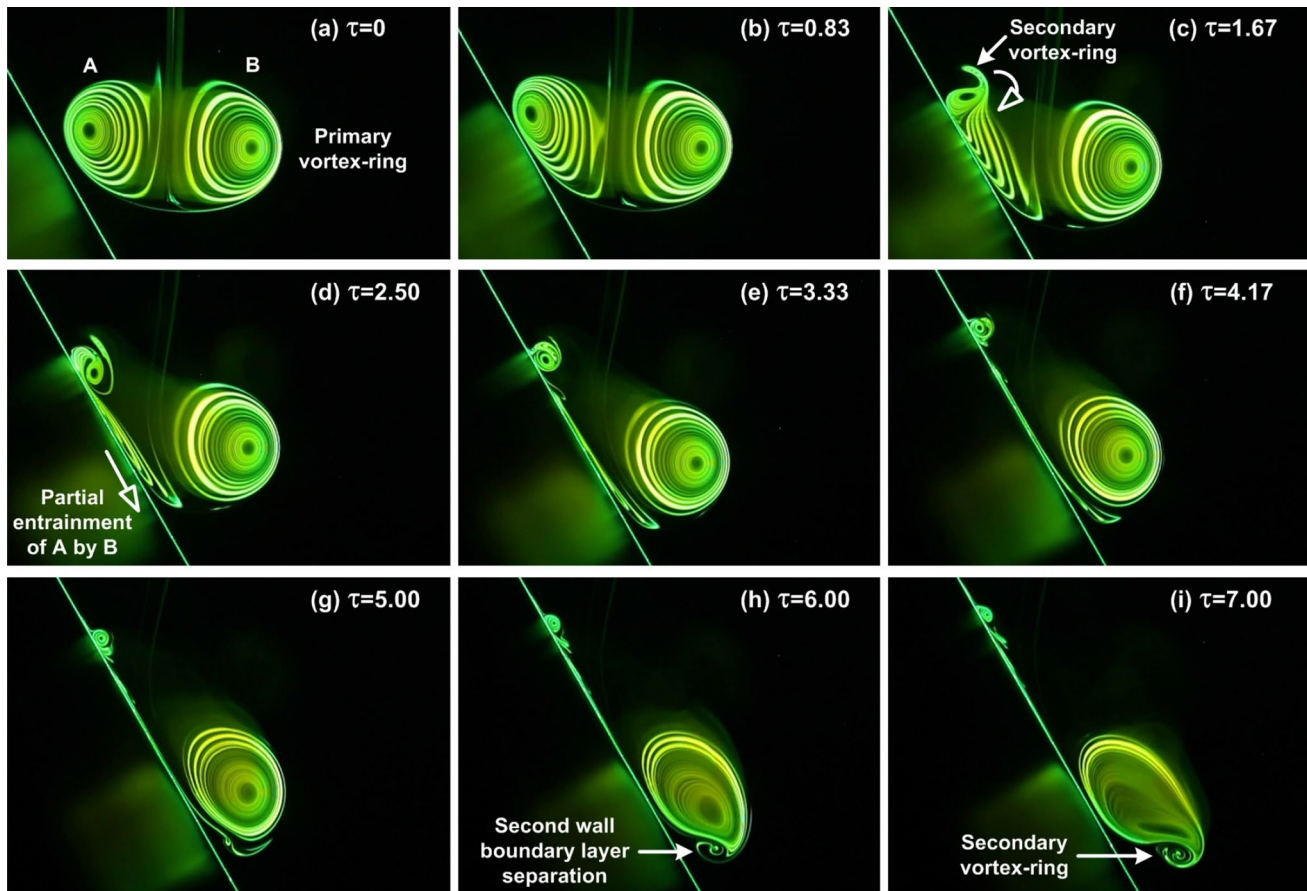


Fig. 7 Instantaneous flow visualizations of $Re = 2000$ vortex-ring collision with 60° inclined flat surface as viewed along the inclined plane

and 60° inclined surfaces are presented, respectively (see “ $Re = 4000$ 30° inclined collision – inclined plane” and “ $Re = 4000$ 60° inclined collision – inclined plane” video clips in Supplementary materials 7 and 8 respectively). It can be observed that increasing the vortex-ring Reynolds number results in similar general flow behaviour as seen earlier but with them occurring in a temporally faster fashion. Furthermore, increasing the inclination angle also leads to the same effects seen previously for $Re = 2000$ vortex-ring collisions. Gross flow similarities can also be observed in the primary and secondary vortex-core trajectories quantitatively tracked from the flow visualization videos for both $Re = 2000$ and 4000 vortex-ring collisions for 30° , 45° , 60° , and 75° inclination angles, as shown in Figs. 11 and 12. Note that the time intervals between the data points in Figs. 11 and 12 are 0.067 s (i.e. every two image frames) and 0.033 s (i.e. every image frame), respectively. A slightly longer time interval is intentionally used for the lower Reynolds test case in Fig. 11 to prevent overcrowding of data points while preserving good tracking of the vortex-core trajectories. It should be highlighted that vortex-core locations and trajectory in Fig. 11a have been compared to those determined from corresponding

vorticity and λ_2 -criterion filtered results, and satisfactory agreements between them had been observed during the comparisons.

Upon closer inspection, some interesting differences can be discerned for the largest inclination angle of 75° . For instance, it is clear from Fig. 11 that the secondary vortex core does not get entrained into the confines of the primary vortex core B when the inclination angle reaches 45° and beyond at $Re = 2000$. This observation can be seen to manifest at $Re = 4000$ as well, with the curious exception of the 75° inclination angle. In this case, the secondary vortex core appears to abruptly turn and travel towards the upstream direction after some distance away from the inclined surface. This behaviour is unlike those seen in Figs. 11b and 12b, where the secondary vortex core turns and travel towards the confines of the primary vortex core immediately once they are formed. To investigate further, Fig. 13 shows the flow visualizations taken for vortex-ring collision with 75° inclined surface at $Re = 4000$ (see “ $Re = 4000$ 75° inclined collision – inclined plane” video clip in Supplementary material 9). Figure 13k–o shows that after the collision, vortex core B and the adjacent secondary vortex core interact such that they form a

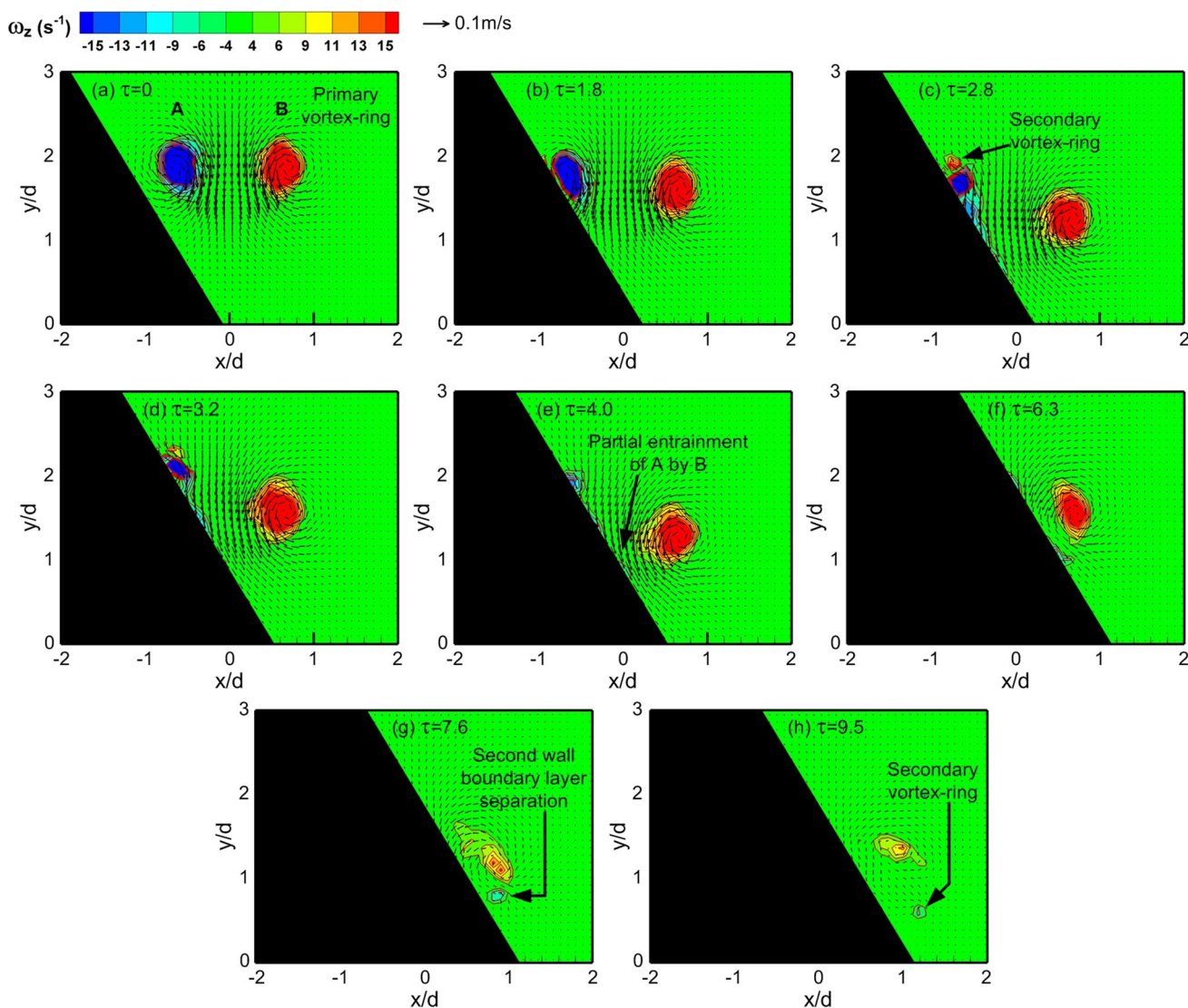


Fig. 8 Instantaneous vorticity maps of $Re = 2000$ vortex ring colliding with 60° inclined flat surface as viewed along the inclined plane

mushroom-shaped vortex dipole that detaches and moves away from the inclined surface almost perpendicularly. The movement away from the inclined surface is also accompanied by a gradual overall rotation such that the vortex dipole turns up towards the inclined surface, as shown in Fig. 13p–t.

The preceding vortical and trajectory behaviour is unlike what has been observed for smaller inclination angles and has in fact been observed previously by Couch and Krueger (2011). Thus, the present results support their observations and indicated that large vortex-stretching effects encountered during vortex-ring collisions with highly inclined flat surfaces may introduce extraneous three-dimensional flow effects not seen at or predicted for smaller inclination angles. This statement is further supported by the persistent presence of a small vortex-ring-like structure further up the

inclined surface close to the top of Fig. 13q–t. It should be mentioned that during the course of the present study, this small vortex-ring-like structure was initially thought to be an extraneous vortical entity resulting from visualization or alignment imperfections associated with the current experiments. However, it consistently appeared in subsequent repeated experiments, even after the experimental apparatus was adjusted several times to correct for any potential alignment imperfections. Comparing Fig. 13 with Figs. 5, 7, 9, and 10, it is clear that this small vortex-ring-like structure does not manifest when smaller inclination angles are used.

In an attempt to have a better idea of what this small vortex-ring-like structure actually is, present DPIV and DDPTV measurements by Couch and Krueger (2011) for their large inclination test cases were consulted. However, no clear evidence can be found in the present or previous

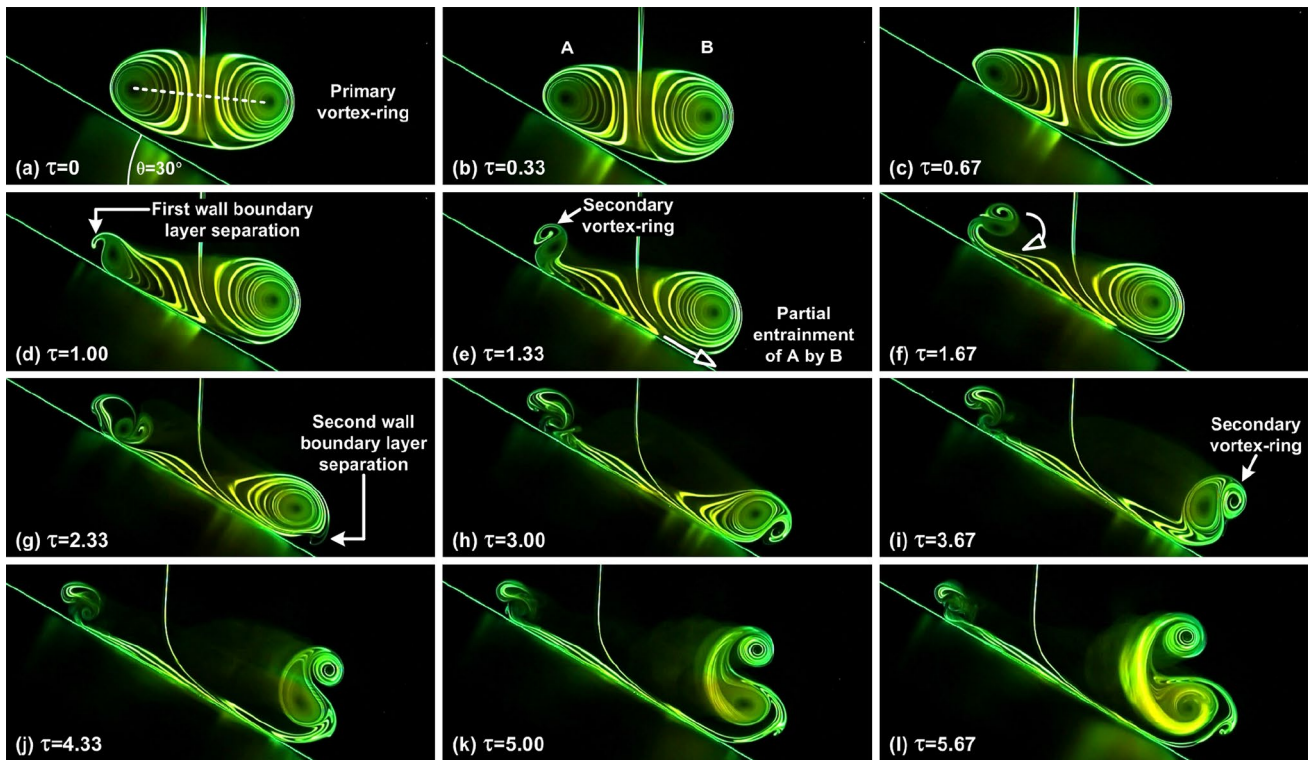


Fig. 9 Instantaneous flow visualizations of $Re = 4000$ vortex-ring collision with 30° inclined flat surface as viewed along the inclined plane

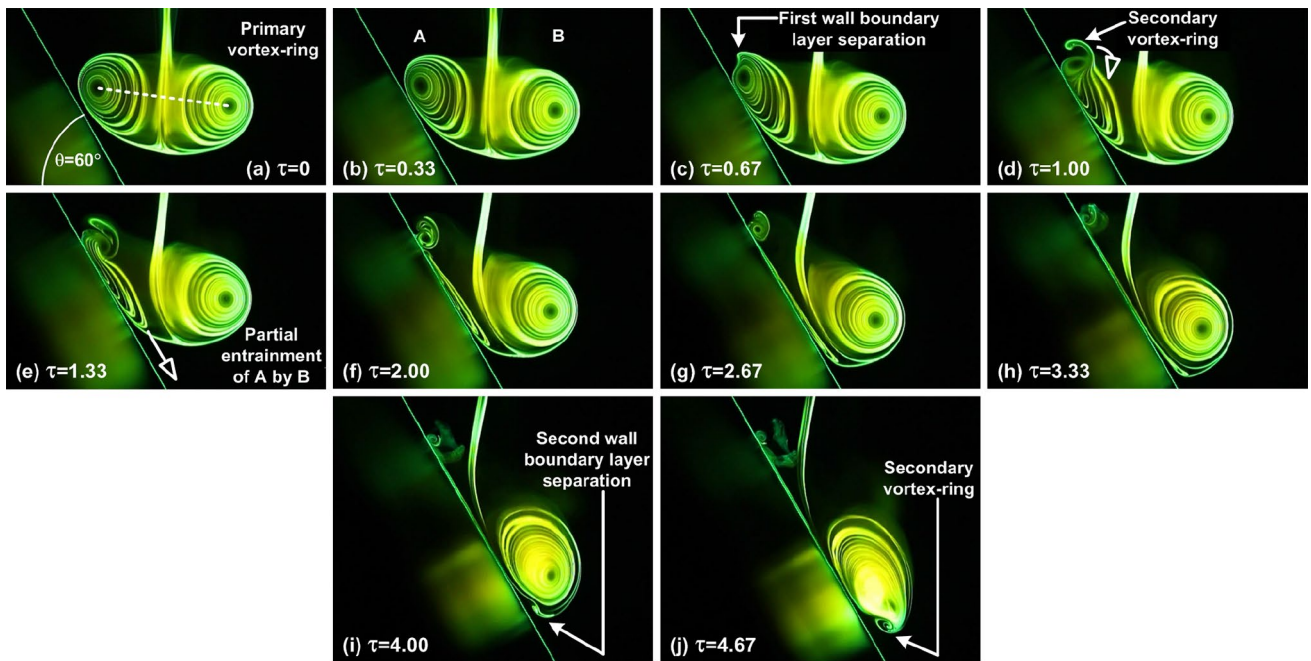


Fig. 10 Instantaneous flow visualizations of $Re = 4000$ vortex-ring collision with 60° inclined flat surface as viewed along the inclined plane

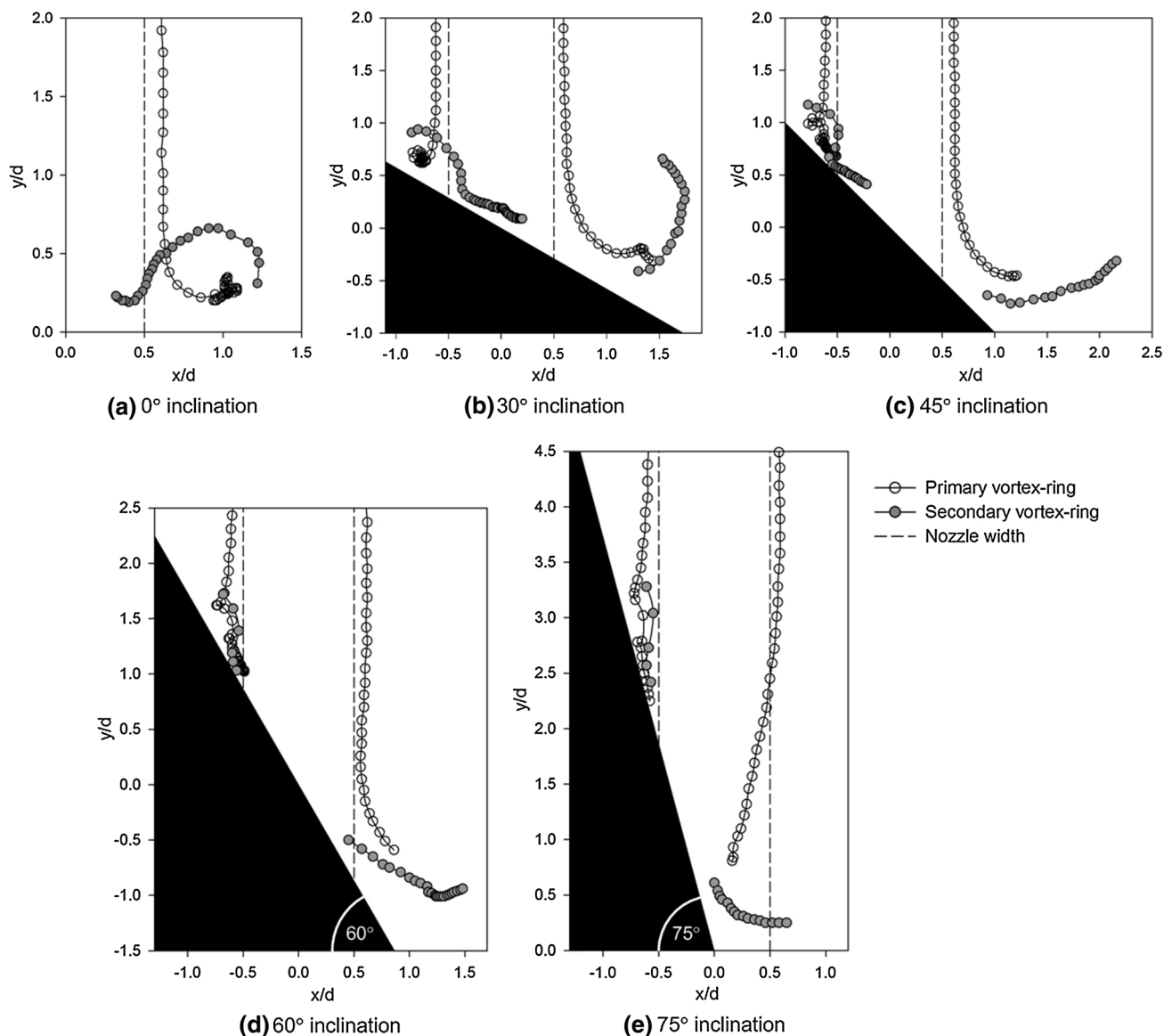


Fig. 11 Primary and secondary vortex-core trajectories for $Re = 2000$ vortex ring colliding upon inclined surfaces

measurement results, though a number of possible explanations exist. Firstly, the small vortex-ring-like structure is expected to be much weaker than the primary and secondary vortex rings and will therefore be difficult to isolate from DPIV vorticity results unless high-resolution or high-magnification measurements were taken. Secondly, DDPTV measurements were only presented for the initial stages of the vortex-ring collision process for their test cases, when the small vortex-ring-like structure would not have been formed yet. Furthermore, the voxel size used in the DDPTV experiments was 8 mm, which may not adequately resolve the significantly smaller-sized vortex-ring-like structure seen in Fig. 13t. Nevertheless, the curious persistence of the small vortex-ring-like structure raises the

possibility that some reorganization of the flow vorticities through vortex disconnection and reconnection processes may take place once the inclination angle and/or Reynolds number exceeds a critical level. A good example will be the resulting “vortex ringlets” observed by Lim and Nickels (1992), where careful flow visualizations reveal the vortex disconnection and reconnection processes associated with head-on collisions of two vortex rings. Heightened vortex-stretching levels at large inclination angles and/or Reynolds numbers are also likely to lead to accentuated vortex-ring dynamics that may be quite different from those postulated based on smaller inclination angles or Reynolds numbers, which should prove to be an interesting topic for further investigations.

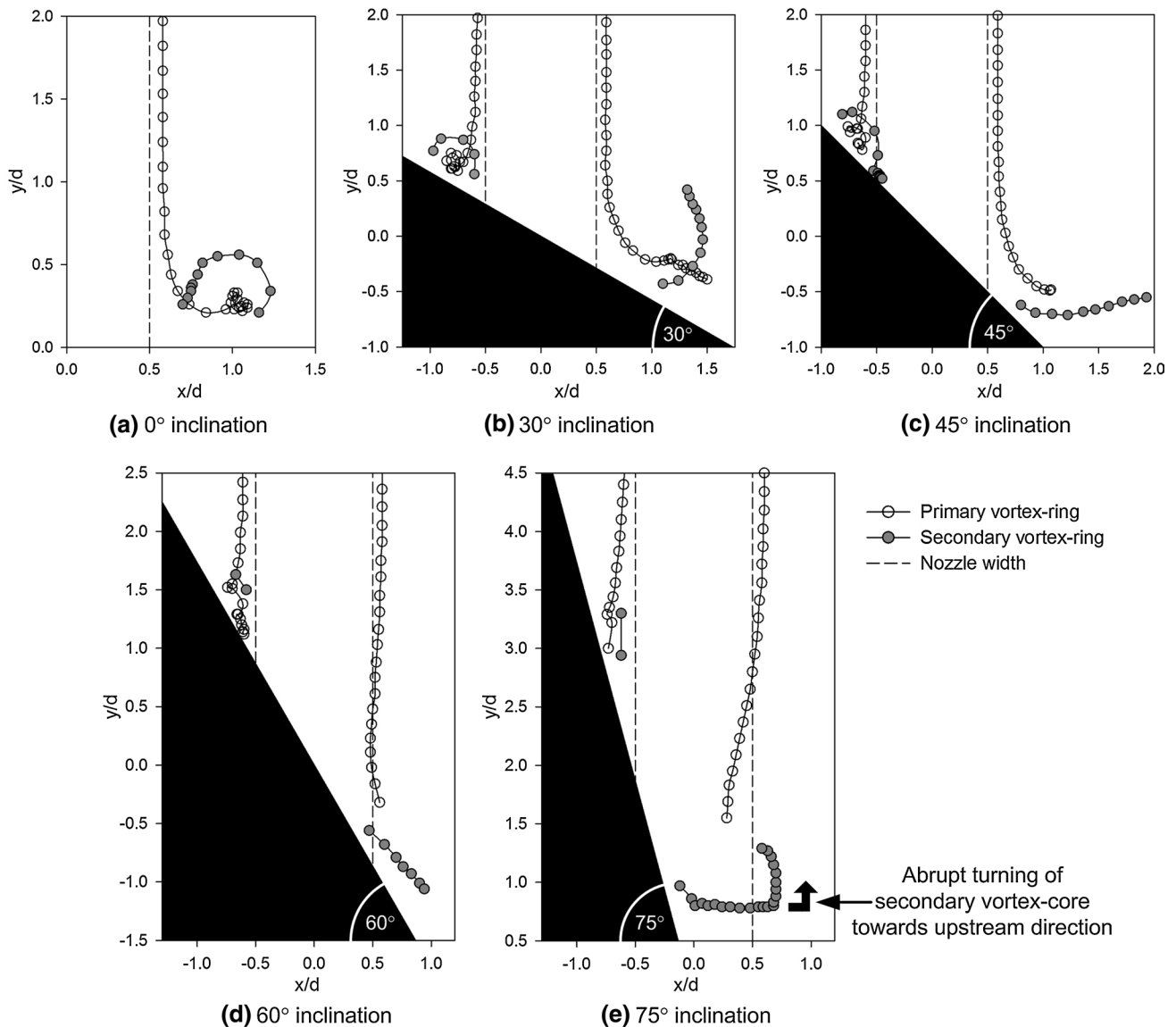


Fig. 12 Primary and secondary vortex-core trajectories for $Re = 4000$ vortex ring colliding upon inclined surfaces

3.4 Collision behaviour along non-inclined plane

Next, flow visualizations and TR-PIV measurements taken along the non-inclined plane will be presented and discussed. However, it should be mentioned that only results for 30° and 60° inclination angles will be presented as gross behaviour for other inclination angles are again relatively similar. Also, since the primary and secondary vortex-core trajectories do not vary as much along this plane as the previous plane, the vortex-core trajectories will not be included and discussed here for the sake of brevity. It can be seen from Figs. 14 and 15 for the 30° inclination angle test case that the general flow behaviour is consistent with those deduced from Fig. 3 earlier (see “ $Re = 2000$ 30° inclined collision – non-inclined plane” and “ $Re = 2000$

30° inclined collision – non-inclined plane TR-PIV” video clips in Supplementary materials 10 and 11 respectively) and hence detailed descriptions of the flow behaviour will not be covered here again. Briefly speaking, the collision of the vortex ring upon the 30° inclined surface leads to the formation of secondary vortex cores that get entrained into the confines of the primary vortex cores, with tertiary vortex cores forming thereafter. It is however particularly interesting to note that the primary vortex-core regions depicted in Fig. 14h, i begin to show the presence of additional vortex cores and associated vortical motions, rather than just those associated with the primary vortex ring as seen in Fig. 4 earlier on. Since only the primary, secondary, and tertiary vortex cores are expected to be observed along this plane, the additional vortex cores are arguably due to

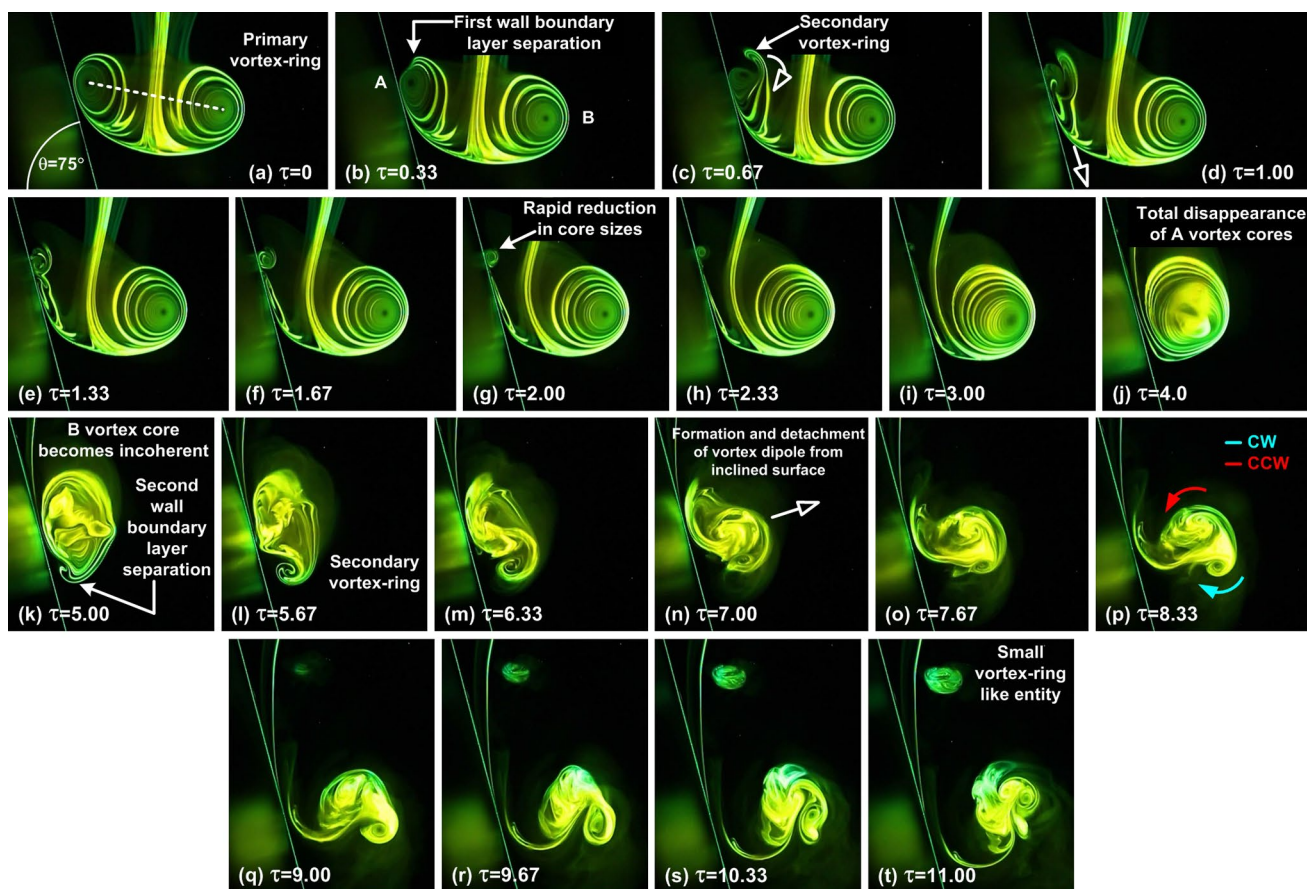


Fig. 13 Instantaneous flow visualizations of $Re = 4000$ vortex-ring collision with 75° inclined flat surface as viewed along the inclined plane

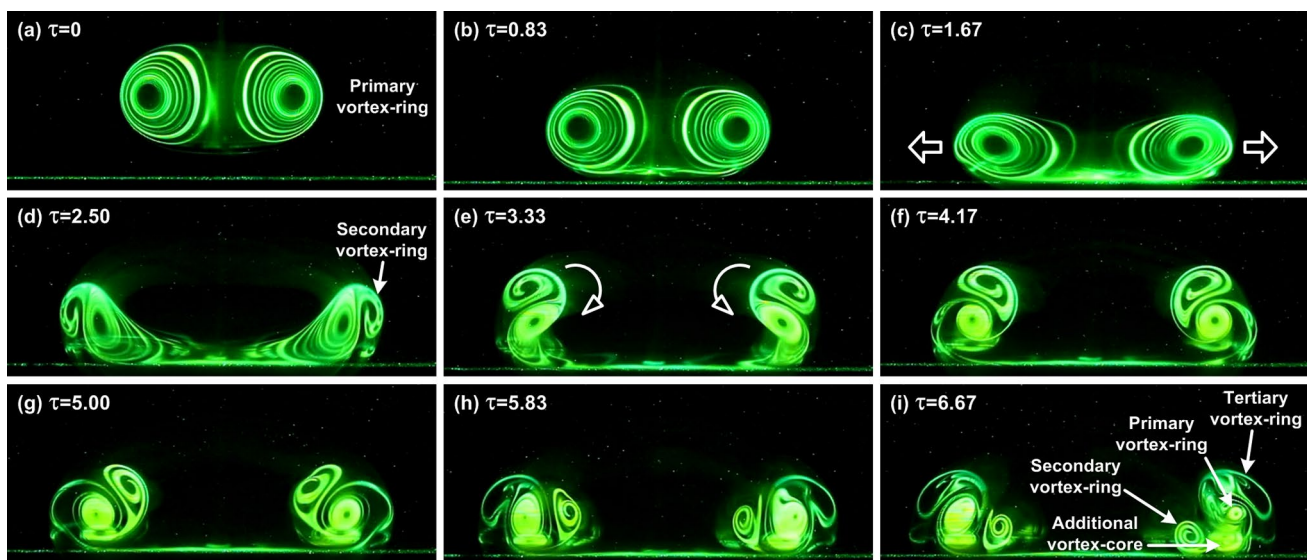


Fig. 14 Instantaneous flow visualizations of $Re = 2000$ vortex-ring collision with 30° inclined flat surface as viewed along the non-inclined plane

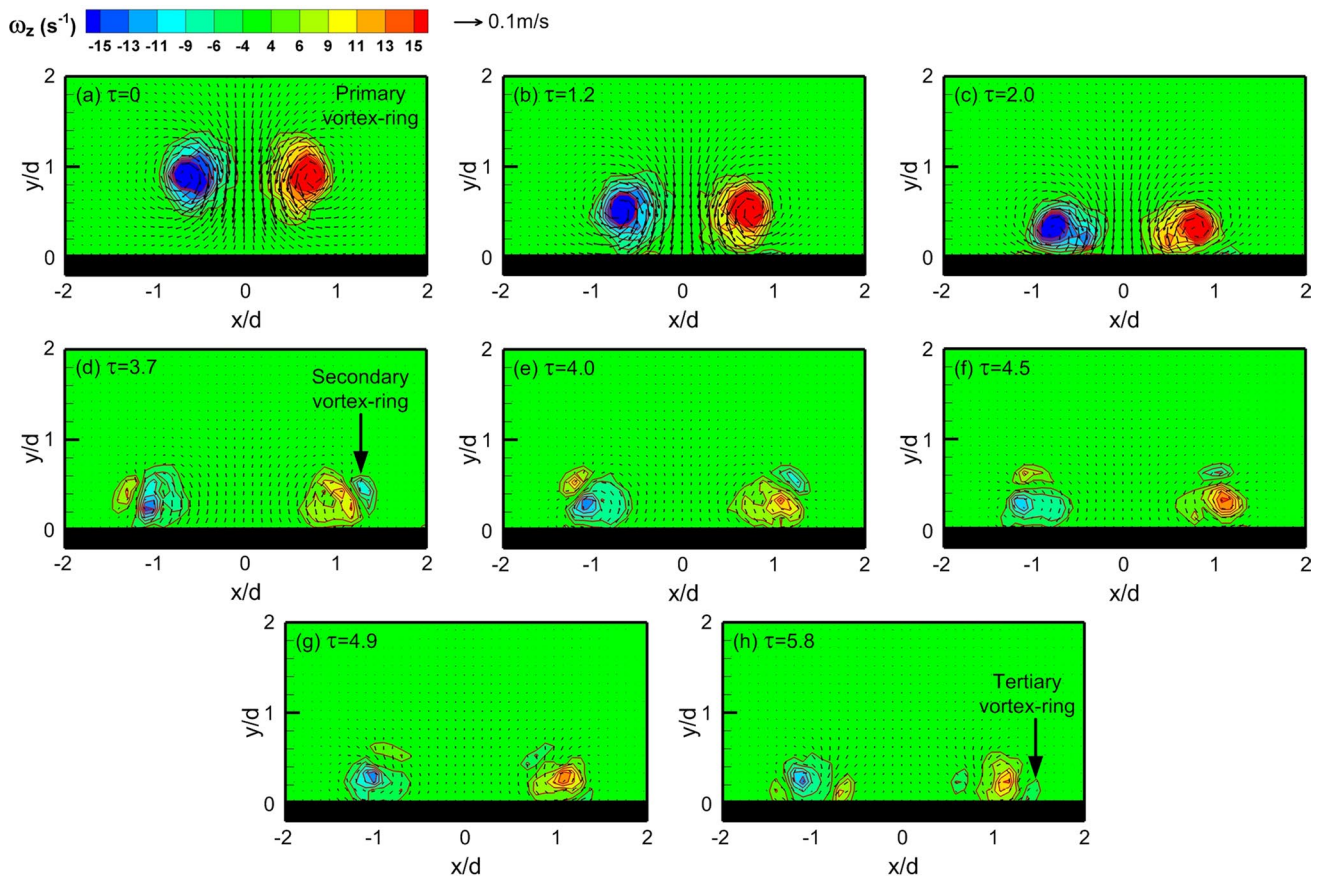


Fig. 15 Instantaneous vorticity maps of $Re = 2000$ vortex ring colliding with 30° inclined flat surface as viewed along the non-inclined plane

the bi-helical vortex lines entwining around the primary vortex-ring filament. Note that Cheng et al. (2010) have also reported the formation of helical structures around the vortex rings in their numerical study.

If that is the case, these images are direct experimental flow visualization evidence in support of the bi-helical vortex line model postulated by Lim (1989), where these additional vortex cores are likely to be the cross sections of the bi-helical vortex lines entwining around the primary vortex-ring filament under flow compression effects. However, it should be reminded that that these additional vortex cores appear relatively late into the collision process, and there is always the possibility that they are the results of extraneous unsteady flow behaviour. Nevertheless, repeated experiments demonstrated that the above-mentioned flow behaviour was always present in both primary vortex-core regions (i.e. left and right regions in the flow visualization images). Hence, that possibility was largely eliminated. If these additional vortex cores are indeed cross sections of the entwining bi-helical vortex lines, it stands to argue that they would manifest again but earlier if the inclination angle were to be increased further, due to even greater vortex-stretching and flow compression effects along

the primary vortex-ring filament. As such, corresponding flow visualization and TR-PIV experiments were conducted for $Re = 2000$ vortex-ring collisions with the 60° inclined surface and are presented in Figs. 16 and 17 (see “ $Re = 2000$ 60° inclined collision – non-inclined plane” and “ $Re = 2000$ 60° inclined collision – non-inclined plane TR-PIV” video clips in Supplementary materials 12 and 13 respectively).

Figure 16a–c shows that the primary vortex cores undergo significant bulging. This bulging results from an even higher level of circumferential flow from vortex core A region towards vortex core B region, and have been observed previously not only in vortex-ring collisions with inclined surfaces, but also in vortex rings forming off inclined nozzles as well (Webster and Longmire 1998; Lim 1998; New 2009; Troolin and Longmire 2010; Le et al. 2011; New and Tsovolos 2011, 2012; Shi and New 2013). It should be mentioned that the secondary vortex core appears to be significantly smaller along this visualization plane (see Fig. 16e, f), presumably due to the high levels of circumferential flow along the primary vortex-ring filament out of the image plane here (and hence vortex-stretching effects), exacerbated by the large inclination angle. Similar

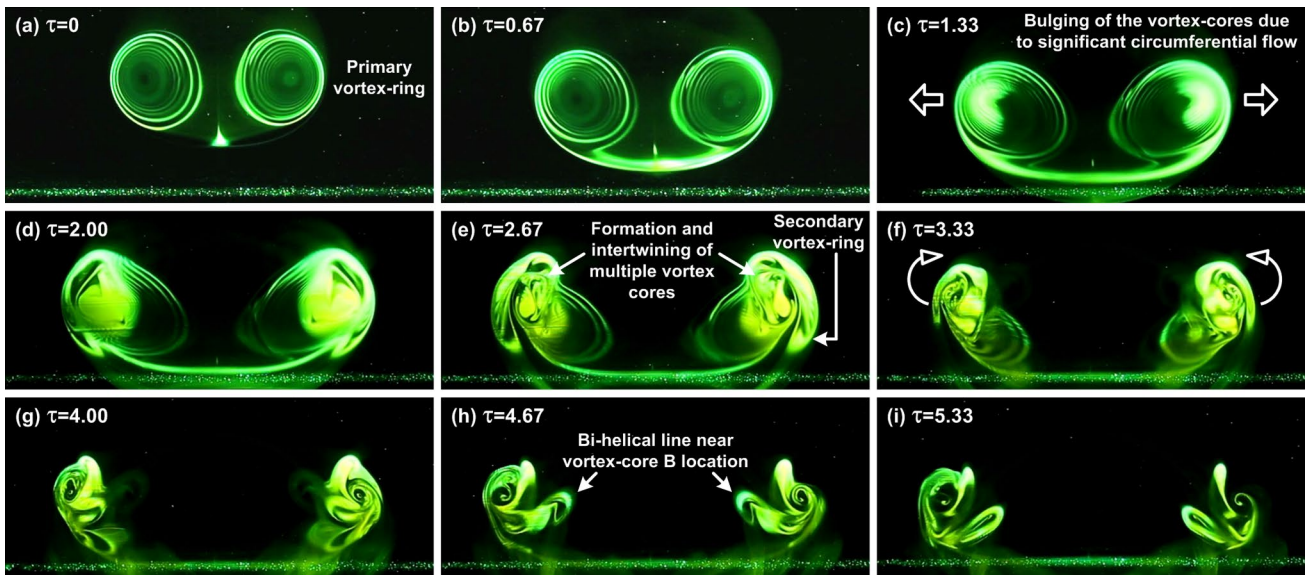


Fig. 16 Instantaneous flow visualizations of $Re = 2000$ vortex-ring collision with 60° inclined flat surface as viewed along the non-inclined plane

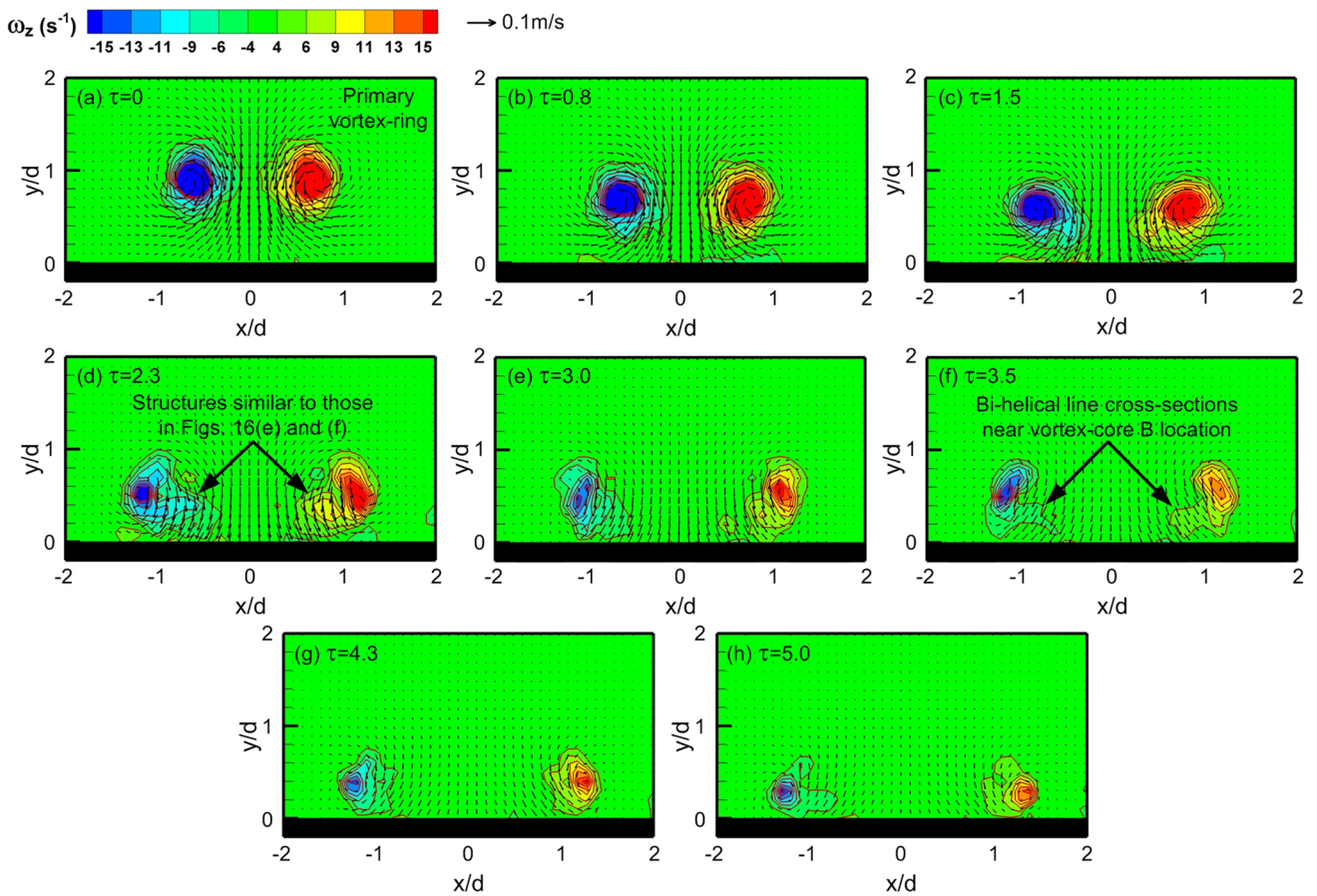


Fig. 17 Instantaneous vorticity maps of $Re = 2000$ vortex ring colliding with 60° inclined flat surface as viewed along the non-inclined plane

to Fig. 14, additional vortex cores are visualized together with the primary vortex cores in Fig. 16e onwards, where they appear to intertwine with one another. This occurs while the weak secondary vortex cores are being formed and prior to their entrainment into the confines of the primary vortex cores.

Furthermore, cross sections of these additional vortex cores can be seen to propagate closer towards the centre of the flow images in Fig. 16h. Recall from the bi-helical vortex line flow model, the bi-helical vortex lines are postulated to gradually bunch up towards the vortex core B region due to the presence of the circumferential flows along the primary vortex-ring filament. If that is the case, cross sections of the associated vortex cores during 2D LIF visualization experiments should in principle move from the primary vortex-ring periphery region towards the centre of the flow images—which is what has been observed here. As such, the present experimental results are certainly in good agreement with that expectation and reinforce the notion that the bi-helical vortex line flow model proposed by Lim (1989) is valid and may be used as a basis to explain more complex vortex-ring collision scenarios.

4 Conclusions

An experimental LIF visualization and TR-PIV measurement study on the collisions of $Re = 2000$ and 4000 circular vortex rings upon surfaces inclined at 30° to 75° had been conducted. Regardless of the Reynolds number, results taken along the inclined plane show that the primary vortex-ring collision leads to the formation and subsequent entrainment of a secondary vortex ring, albeit much more rapid for the primary vortex-ring segment closer to the inclined surface. Formation of tertiary vortex rings becomes impeded or absent when the inclination angle reaches 60° and beyond. Close examination of the primary and secondary vortex-ring core trajectories reveals that they are grossly similar, though those of the higher Reynolds number test case show a temporally faster scenario where the vortex-ring cores closer to the inclined surfaces diminish faster. Interestingly, at the largest inclination angle of 75° and Reynolds number of $Re = 4000$ studied here, vortex-ring cores furthest away from the inclined surface produce a distinct mushroom-shaped vortex dipole that detaches itself away from the inclined surface and undergoes an abrupt change in its trajectory. A small vortex-ring-like structure is also consistently observed to accompany the formation of the vortex dipole, but located further up the inclined surface. At this point in time, it is postulated that this small vortex-ring structure may be a result of vortex disconnection–reconnection processes produced under very large inclination angles.

Lastly, results taken along the non-inclined plane reveal that increasing the inclination angle from 30° to 60° leads to a growth in circumferential flow along the primary vortex-ring filament and subsequent bulging of the primary vortex-ring cores. Formation and entrainment of secondary vortex ring by the primary vortex ring can also be discerned from the flow results. However, the secondary vortex-core sizes become significantly smaller at an inclination angle of 60° , presumably due to increased vortex-stretching effects. More importantly however, the results demonstrate the direct presence of additional vortex cores that intertwine with the primary vortex-ring cores, which have not been reported in detail before the present study. Their presence and vortical changes as reflected in the experimental results are found to support the bi-helical line flow model put forward by Lim (1989) for circular vortex rings colliding with inclined surfaces.

Acknowledgments The authors gratefully acknowledge the support for this study by the Nanyang Technological University Start-Up Grant, Tan Chin Tuan Exchange Fellowship in Engineering, as well as China NSFC Grant (51106096). Assistance in the flow visualization experiments from Wang L. and Kong M. at Shanghai Jiao Tong University, and programming of the stepper motor by Kwan Z. R. are also greatly appreciated.

References

- Adhikari D, Lim TT (2009) The impact of a vortex ring on a porous screen. *Fluid Dyn Res* 41:051404
- Cheng M, Lou J, Luo L-S (2010) Numerical study of a vortex ring impacting a flat wall. *J Fluid Mech* 660:430–455
- Chu CC, Wang CT, Chang CC (1995) A vortex ring impinging on a solid plane surface—vortex structure and surface force. *Phys Fluids* 7:1391–1401
- Couch LD, Krueger PS (2011) Experimental investigation of vortex rings impinging on inclined surfaces. *Exp Fluids* 51:1123–1138
- Fabris D, Liepmann D, Marcus D (1996) Quantitative experimental and numerical investigation of a vortex ring impinging on a wall. *Phys Fluids* 8:2640–2649
- Gharib M, Rambod E, Shariff K (1998) A universal time scale for vortex ring formation. *J Fluid Mech* 360:121–140
- Homa J, Lucas M, Rockwell D (1988) Interaction of impulsively generated vortex pairs with bodies. *J Fluid Mech* 197:571–594
- Hrynyuk JT, Van Luipen J, Bohl D (2012) Flow visualization of a vortex ring interaction with porous surfaces. *Phys Fluids* 24:037103
- Jang IS, Chiba H, Watanabe S (1996) Impact of a vortex ring on a wall in high Reynolds number region. *J Phys Soc Jpn* 65:955–959
- Keane RD, Adrian RJ (1992) Theory of cross-correlation analysis of PIV images. *Appl Sci Res* 49:191–215
- Krueger PS, Gharib M (2003) The significance of vortex ring formation to the impulse and thrust of a starting jet. *Phys Fluids* 15:1271–1281
- Le TB, Borazjani I, Kang S, Sotiropoulos F (2011) On the structure of vortex rings from inclined nozzles. *J Fluid Mech* 686:451–483
- Lim TT (1989) An experimental study of a vortex ring interacting with an inclined wall. *Exp Fluids* 7:453–463
- Lim TT (1998) On the breakdown of vortex rings from inclined nozzles. *Phys Fluids* 10:1666–1671

- Lim TT, Nickels TB (1992) Instability and reconnection in the head-on collision of two vortex rings. *Nature* 357:225–227
- Lim TT, Nickels TB, Chong MS (1991) A note on the cause of rebound in the head-on collision of a vortex ring with a wall. *Exp Fluids* 12:41–48
- Luff JD, Drouillard T, Rompage AM, Linné MA, Hertzberg JR (1999) Experimental uncertainties associated with particle image velocimetry (PIV) based vorticity algorithms. *Exp Fluids* 26:36–54
- Minota T, Nishida M, Lee MG (1997) Shock formation by compressible vortex ring impinging on a wall. *Fluid Dyn Res* 21:139–157
- Naaktgeboren C, Krueger PS, Lage JL (2012) Interaction of a laminar vortex ring with a thin permeable screen. *J Fluid Mech* 707:260–286
- Naitoh T, Banno O, Yamada H (2001) Longitudinal vortex structure in the flow field produced by a vortex ring impinging on a flat plate. *Fluid Dyn Res* 28:61–74
- New TH (2009) An experimental study on jets issuing from elliptic inclined nozzles. *Exp Fluids* 46:1139–1157
- New TH, Tay WL (2006) Effects of cross-stream radial injections on a round jet. *J Turb* 7:N57
- New TH, Tsovolos D (2009) Influence of nozzle sharpness on the flow fields of V-notched nozzle jets. *Phys Fluids* 21:084107
- New TH, Tsovolos D (2011) On the vortical structures and behaviour of inclined elliptic jets. *Eur J Mech B Fluids* 30:437–450
- New TH, Tsovolos D (2012) On the flow characteristics of minor-plane inclined elliptic jets. *Exp Therm Fluid Sci* 38:94–106
- New TH, Shi S, Liu Y (2013) Cylinder-wall interference effects on finite-length wavy cylinders at subcritical Reynolds number flows. *Exp Fluids* 54:1601
- Orlandi P (1990) Vortex dipole rebound from a wall. *Phys Fluids A* 2:1429–1436
- Orlandi P, Verzicco R (1993) Vortex rings impinging on walls: axisymmetric and three-dimensional simulations. *J Fluid Mech* 256:615–646
- Shi S, New TH (2013) Some observations in the vortex-turning behaviour of noncircular inclined jets. *Exp Fluids* 54:1614
- Shi S, New TH, Liu Y (2013) Flapping dynamics of a low aspect-ratio energy-harvesting membrane immersed in a square cylinder wake. *Exp Therm Fluid Sci* 46:151–161
- Swearingen JD, Crouch JD, Handler RA (1995) Dynamics and stability of a vortex ring impacting a solid boundary. *J Fluid Mech* 297:1–28
- Troolin DR, Longmire EK (2010) Volumetric velocity measurements of vortex rings from inclined exits. *Exp Fluids* 48:409–420
- Verzicco R, Orlandi P (1994) Normal and oblique collisions of a vortex ring with a wall. *Meccanica* 29:383–391
- Walker JDA, Smith CR, Cerra AW, Doligalski TL (1987) The impact of a vortex ring on a wall. *J Fluid Mech* 181:99–140
- Webster DR, Longmire EK (1998) Vortex rings from cylinders with inclined exits. *Phys Fluids* 10:400–416